9th U. S. National Combustion Meeting
Organized by the Central States Section of the Combustion Institute
May 17-20, 2015
Cincinnati, Ohio

Comparing Vapor Penetration Measurements from IR Thermography of C-H Stretch with Schlieren during Fuel Injection in a Heavy-Duty Diesel Engine

W. Ethan Eagle[1], Louis-Marie Malbec[2], and Mark P.B. Musculus[1]

[1]Engine Research Department, Combustion Research Facility, Sandia National Labs, Livermore, USA
[2]IFPEN, Rueil-Malmaison, France
[*]Corresponding Author Email: weeagle@sandia.gov

Abstract: Simplified mixing-limited spray-vaporization models can successfully predict liquid length and vapor-fuel concentrations when the penetration rate or spreading angle is a known input. Traditional techniques to measure the jet spreading angle and/or vapor-phase penetration, such as back-lit shadowgraph, schlieren, or laser-induced fluorescence, require a combustion chamber with multiple ports for optical access. This access may be provided by an optical constant-volume vessel or an optical-piston engine with line-of-sight access through the cylinder head and/or cylinder wall. One attractive alternative for measuring fuel-vapor penetration and spreading angle requiring only a single window for optical access is infrared (IR) thermography. Thermal emission from the C-H stretch band near a wavelength of 3.4 microns indicates the presence of hot hydrocarbon fuel, which has been heated by mixing with compressed ambient gases, typically at 700 K or higher during fuel injection. Additionally, because the IR technique is direct line-of-sight, simultaneous measurement of multiple fuel jets is trivial. To interpret the IR emission signals, the relative contributions of local vapor-fuel concentration and temperature to the signals are estimated using a one-dimensional axisymmetric transient jet model that assumes adiabatic mixing. Using an optical heavy-duty diesel engine, fuel-vapor penetration detected from IR emission imaging of all three jets of the Engine Combustion Network 'Spray B' injector are compared with boundaries from one jet (hole 3) measured using the schlieren technique. IR data is acquired at 0%, 4%, and 15% O_2. Schlieren data are available in the engine at 0% and 4% O_2. From these data, fuel-vapor penetration in the engine appears to be at first slower but then faster than previously published penetration data from a single-hole version of the injector (Spray A) in a constant-volume chamber. The impact of low-temperature reaction on vapor penetration measured between schlieren and IR is also addressed.

Keywords: mid-wave infrared, optical diagnostics, diesel engine

1. Introduction

For understanding in-cylinder processes affecting performance and emissions in direct-injection engines, diagnostics providing spatial and temporal information on fuel mixing rates, the sites of ignition, and the completion of combustion are all of interest. Optical diagnostics to provide information on the mixing and concentration fields for both reacting and non-reacting flows typically combine lasers and/or detectors in the visible and ultraviolet (UV) wavelengths. These include: elastic Mie scattering and schlieren or shadowgraph techniques to measure the liquid- and/or vapor-fuel penetration; Rayleigh scattering or laser-induced fluorescence (LIF) of doped tracers to measure vapor-fuel concentration; OH* chemiluminescence (strongest near the

stoichiometric contour) or LIF of intermediate species to track ignition and the progression of combustion; and other techniques, see e.g. Alden et al. (2011). These techniques have provided a wealth of information about mixing and combustion processes, both for single-shot and ensemble-averaged measurements. To make dynamic measurements at reasonable engine crankshaft speeds of 1200-2400 rotations per minute (RPM), single-cycle time-resolved imaging requires detection speeds at or above 1 image per crank-angle degree (CAD), which corresponds to 7200-14400 frames per second (fps). For detailed fuel-jet penetration, temporal resolutions of 100,000fps are increasingly common (Eagle, Morris, and Wooldridge 2014). Laser-based diagnostics can be limited by repetition rate, power, and shot-to-shot variability. Open challenges remain in the analysis of engine data, particularly in cycle-to-cycle variation, and the limitations in available laser energy and laser repeatability may be encountered when attempting to obtain, for example, cycle-resolved detection of vapor penetration.

A viable method for time-resolved fuel-vapor penetration that does not necessarily require a laser source is a schlieren or shadowgraph technique. These function when strong refractive-index gradients in the fuel jet deflect a beam of propagating visible light en-route to the detector. To achieve detection at high speed requires high-flux light sources. Previously these included mercury arc-lamps, diffused halogen floodlight, and lasers, as discussed in textbooks on the methods, see e.g. Settles (2001). At high temporal resolutions (above 20kHz), the speed, variability, and/or cost of these sources can become problematic. With recent advances, low-cost light-emitting diode (LED) technology can provide repeatable, uniform, short-duration pulses (in some cases sub-microsecond bursts) of diffuse or collimated back light (Blessinger et al. 2014). Nevertheless, application of the schlieren or shadowgraph techniques still requires pass-through optical access and flat windows[*].

Providing optical access while maintaining production, or near-production geometry, remains a non-trivial aspect of an experimental design. Significant effort is required to design and operate engines with all-optical liners, or port-cut outs that provide the optical access for laser diagnostics. And for certain processes like jet penetration, direct-injection soot formation, and ignition locations, where unfettered optical access is needed, experiments are often performed in surrogate environments like constant-volume combustion chambers and rapid-compression machines. However, the transient behavior of the engine (particularly cylinder expansion and flows induced by the crank-slider motion of the piston geometry) is lost. Therefore techniques are desirable that can be readily applied in an engine environment without requiring significant modification for optical access and are capable of detecting vapor fuel over a wide range of concentrations, particularly for low concentrations at the boundary of the penetrating jet. Detection of infrared (IR) emission may be one such method.

Early work in flame spectroscopy indicated the possibility for the detection of fuel vapor and combustion intermediates at the near and mid IR wavelengths (Agnew, Agnew, and Wark 1955). Spectroscopic reference databases like HITRAN can be consulted for various atmospheric species transmittance (Rothman et al. 1998) to determine useful wavelength detection ranges. Preliminary studies of IR flame-emission in engines using two 64x64 PtSi detectors at 1800fps gave 2CAD resolution and demonstrated four-band (2.2, 2.47, 3.42, and 3.8 microns) IR imaging over the full bowl for a spark-ignition engine, and through an intake valve in a 1.85L single-cylinder compression-ignition engine (Jansons et al. 2000). Detailed features of the piston crown

[*] In schlieren experiments, an additional cylindrical lens in the beam path can sometimes compensate for curvature in a single direction, but not compound curvature, see e.g. [Settles 2001]

or engine head are not apparent in the published images, perhaps indicating a narrow detector dynamic range at low exposure times (embodied by either lack of sensitivity or lack of bit depth) using the IR imaging technology available at that time. In other studies, fuel emission-spectra were measured for temperatures between 300 and 700K and up to 2Mpa (Tomita, Kawahara, and Nishiyama 2003; Klingbeil, Jeffries, and Hanson 2007). These results collectively demonstrate a strong hydrocarbon absorption band at wavelengths between 3.3 and 3.5 microns associated with vibrational transitions of the C-H bond stretch. Tomita further argued that the emission strength of the C-H stretch varies nearly linearly with the number of CH_2 groups. Building on these efforts, spectroscopic studies of pre-flame regions in a direct-injection engine indicate the viability of the 3.4 micron band for detection of fuel vapors, and show through HITRAN modeling that such measurements should be nearly free of interference from non-fuel species (Jansons, Lin, and Rhee 2008).

Recent improvements to indium antimonide (InSb) detector response times, sensitivities, and bit depth has opened the door to new detection methods with improved dynamic range, including line-of-sight dual-band IR absorption for residual gas concentration (Kawahara et al. 2011), for simultaneous quantitative concentration and temperature (Klingbeil et al. 2009), and for full-field qualitative fuel-vapor IR emission imaging (Squibb et al. 2011; Mancaruso, Sequino, and Vaglieco 2014; Mancaruso, Vaglieco, and Sequino 2015), as well as quantitative surface temperature measurements (Schulz et al. 2014; Luo, Yu, and Jansons 2015). Improved dynamic range is evidenced by the clarity of valve and injector features on the engine head, but so far these data have generally only been used to gain a qualitative picture of the IR emission. One exception for jet penetration is an attempt by Mancaruso (2014) to quantify ensemble-averaged IR vapor penetration for the analysis of in-cylinder processes using emission near 3.9 microns rather than 3.4 microns. These data were presented alongside visible Mie scattering from the liquid fuel spray from a high-speed camera, as well as full-spectrum IR detected from 1-5 microns. Quantitative comparisons of penetration were offered only for the first 1.5 CAD after the start of injection, and the relationship between jet penetration measured by IR emission imaging versus other established techniques was not explored.

One thing yet to be established is an explanation (or comparison) of the how the vapor-fuel IR emission signal is indicative of vapor penetration. Furthermore, a comparison of the detected penetration from IR imaging with other metrics including schlieren has not been pursued. Here we demonstrate progress in both areas. This paper begins with an overview of predicted IR emission from vapor fuel during injection and its detection in the C-H stretch band near 3.4 micron wavelength. A quasi 1-dimensional (1-d) diesel fuel-jet model (Musculus and Kattke 2009) is used to estimate the ensemble-averaged fuel concentrations and temperatures to estimate how the IR emission signals relate to local fuel concentrations and hence jet penetration. An estimate for the IR emission signal is based on line-of-sight integration of IR emission through the fuel jet. We describe the experimental setup before providing qualitative images of fuel injection from the three-hole Spray B injector (details below) acquired from a demonstration IR camera on temporary loan. The measured vapor penetration is compared with schlieren measurements of this injector made for the first time in the engine and with penetration data available from the Engine Combustion Network for Spray A, an identical injector with a single axial hole (Picket 2014). Unfortunately, operating conditions for the available data are not identical, so the jet penetration data from various experiments are scaled based on well-established dependencies on injection pressure, orifice size and ambient density (Naber and Siebers 1996). In addition, we confirm previously reported ‘softening’ (Skeen, Manin, and

Pickett 2015) of schlieren images during low temperature reactions even with negligible heat release (only 4% O_2 in the ambient gases) that interferences with the penetration measurements, and show that IR penetration measurement does not exhibit the same degree of sensitivity. In the last section we demonstrate a qualitative increase in the dynamic range and resolution using a recently acquired state-of-the-art IR camera. In these images we see increased IR emission near the injector, apparently due to combustion and/or increased entrainment after the end of injection that further heats the fuel vapors, as noted in other work (Eagle et al. 2014, Knox and Genzale 2015). We close with expected future work, and a summary of key results.

2. Infrared Gas Spectra

Thermal-vibrational radiation of tri-atomic molecular groups arises due to a dipole moment and can be one of six types: symmetric stretch, asymmetric stretch, scissoring, rocking, wagging, and twisting (Bekefi and Barrett 1982). Measurements of fuels with tri-atomic CH_2 groups show a strong absorption feature due to C-H asymmetric stretch centered near 3.4 micron wavelength, or equivalent wavenumber of 2926cm^{-1} (Tomita, Kawahara, and Nishiyama 2003). For quantitative vapor-penetration, the choice of wavelength for detection of fuel vapor should be free of interference from other spectra (in particular H_2O and CO_2[†]). Measured IR absorption spectra of common atmospheric gasses can be found in numerous references, e.g. Rothman et al. (1998). The 3.4 micron band is well isolated from most other emitting species, with the exception of some overlap with H_2O on the short-wavelength side of the band.

The detection wavelength also must be transmissible through the windows (e.g., fused silica or sapphire) of the optical engine. IR transmission through optical materials is strongly dependent on the mix of impurities in the sample. For example, Sapphire and 'IR grade' fused silica from one vendor maintains high transmission up to 3.9 microns, while 'optical grade' fused silica is generally opaque in the IR, though it has a narrow band with partial transmission near 3.4 microns (Janis.com 2015). Fortuitously, the ultraviolet-grade fused silica used our optical engine has transmission above 80%[‡] between 3.3 and 3.5 microns. Hence, the thermal C-H stretch-band emission from hot fuel is relatively well isolated and detectable using our optical engine facility without making any changes to the existing fused silica windows.

3. Infrared Emission Estimation

Quantitative use of the IR has thus far been limited to absorption diagnostics, e.g. Klingbeil et al. (2009). Quantitative measurements using line-of-sight absorption require the knowledge of the fuel's absorptivity, α. For a detailed derivation of the governing equations for line-of-sight absorption measurements, see e.g. Klingbeil, Jeffries and Hanson (2007). For quantitative emission measurements, the treatment for absorption must be modified to account for self-emission from the hot fuel and subsequent self-absorption along the line of sight, as detailed in the following derivation.

Starting with the absorption component, for which scattering may be neglected in the vapor phase, the transmissivity can be evaluated according to Beer's law. The transmissivity, which is the ratio of the transmitted intensity, I, at a given wavelength, λ, to the initial intensity, $I_{\lambda,o}$, can be related to a temperature (T) dependent absorption cross-section, $\sigma_{\lambda,T}$, the molar concentration, N, and the path length, L, as:

[†] Note that symmetric molecules like N_2 and O_2 have no dipole moment, so they are inactive in the IR.
[‡] For 10mm path length

$$\tau_\lambda = {}^{I_\lambda}/_{I_{\lambda,o}} = \exp(-\sigma_{\lambda,T} NL) \quad (1)$$

The absorptivity sums to unity with the transmissivity, so the absorptivity is:

$$\alpha_\lambda = 1 - \tau_\lambda = 1 - \exp(-\sigma_{\lambda,T} NL) \quad (2)$$

The emission component can be quantified using the emissivity of the gas relative to a blackbody. The spectral blackbody radiation intensity, $I_B(T)$, (power per unit area per wavelength per steradian) can be expressed as Planck's equation:

$$I_B(T) = \frac{C_1}{\lambda^5\left[\exp\left(\frac{C_2}{\lambda T}\right)-1\right]} \quad (3)$$

where C_1 and C_2 are Planck's first and second constants. By Kirchoff's law, the emissivity of a gas is equal to the absorbtivity. Hence, from Eq. (1):

$$\varepsilon_\lambda = \alpha_\lambda = 1 - \exp\left(-\sigma_{\lambda,T} N_i L\right) \quad (4)$$

For a differential element along the detection line of sight, the differential change in intensity dI_λ across a differential distance along the line of sight dL can be written according to Swarzchild's equation for radiative transfer as the sum of absorption and emission components:

$$dI_\lambda = -\alpha_\lambda I_\lambda + \varepsilon_\lambda I_B(T) = \left[1 - \exp\left(-\sigma_{\lambda,T} N dL\right)\right](I_B(T) - I_\lambda)^{\S} \quad (5)$$

Using first-order backward differencing, Eq. (5) can be discretized as

$$I_{\lambda,i} = I_{\lambda,i-1} + \left[1 - \exp\left(-\sigma_{\lambda,T_i} N_i \, \Delta L\right)\right]\left(I_B(T_i) - I_{\lambda,i-1}\right) \quad (6)$$

where $I_{\lambda,i}$ is the intensity at discrete element i with length ΔL along the line of sight of length, at concentration, N_i, and $I_{\lambda,i-1}$ is the intensity at the previous element along the line-of-sight. The total emission intensity along a line-of sight can be estimated by numerically integrating Eq. (6) for a discretized series of elements along the line of sight.

To solve Eq. (6), both the local temperature and concentration of the vapor fuel along the line of sight are required. Here, the ensemble-averaged local fuel concentration is estimated using the validated 1-d diesel jet model described elsewhere (Musculus and Kattke 2009), and the ensemble-averaged local temperature is estimated using an adiabatic mixing assumption that accounts for fuel vaporization and sensible heat capacity. The assumptions used in this model have been previously validated (Pickett et al. 2012). Using these, the we

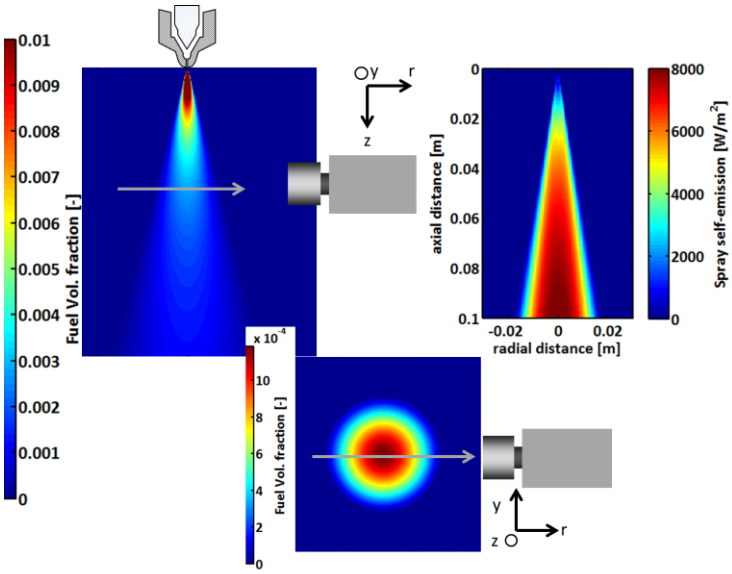

Figure 1 Steady mixing simulation for predicting IR emission. (Left) Fuel concentration profiles in a cross-section along the jet axis. An arrow indicates a line of sight transverse to the jet axis. (Bottom center) Fuel concentration profiles in a cross-sectional orthogonal to the jet axis. (Right) Line-of-sight integrated IR emission for an absorption cross-section of 70 m^2/mol.

§ This is equivalent with previous formulations when dL is small enough, since $1 - \exp(x) = x$ for small x.

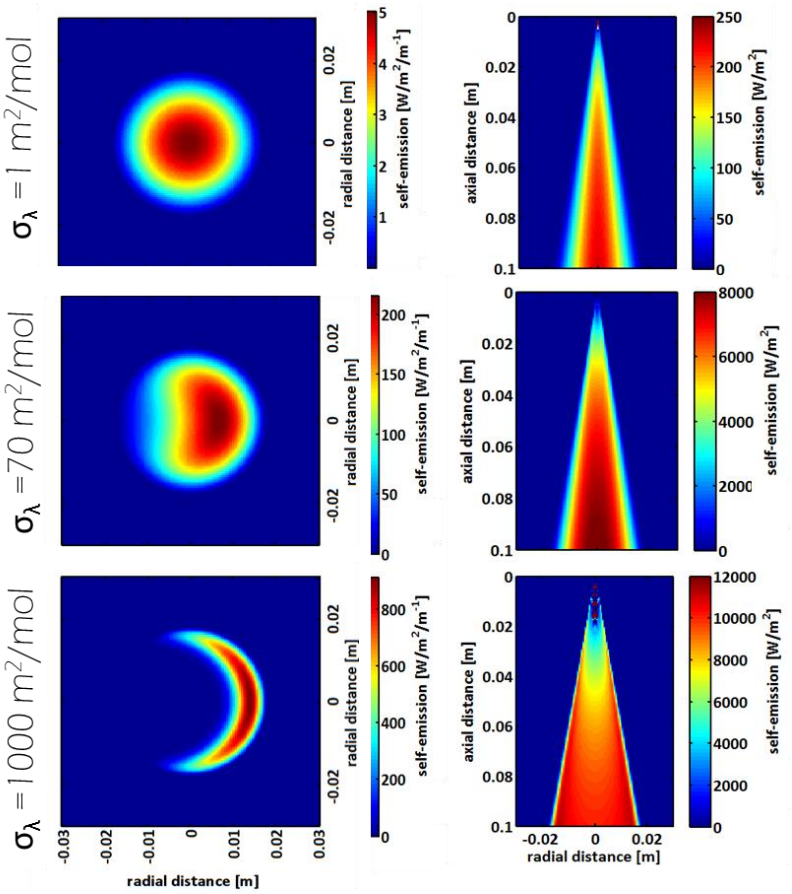

Figure 2 Fuel absorptivity increases from top to bottom for three simulations of IR emission. (Left) Cross section view of the distribution of self-emission that reaches the detector along a path traveling left to right that demonstrates the effect of self-absorption where detection becomes biased to fuel closest to the detector. (Right) Integrated signal reveals sharpener gradients at larger absorption cross section.

present a predicted IR emission distribution along lines of sight transverse to the jet axis (i.e., path length L is along the direction r) in Figure 1.

In Figure 2, the effect of emissivity is examined in terms of the example values for absorption cross section σ_λ, for a very wide range from 1 to 1000m^2/mol. Although the smooth fuel-vapor distribution predicted by the 1-d model is a valid approximation only in the ensemble average, an important tradeoff is evident, that of concentration and temperature. For the range of fuel absorption cross sections measured from Klingbeil (2007) and Tomita (2003) of 0.8-70m^2/mol there will be increasingly strong signal from low concentration regions at the borders of the jet. The chosen value of 70m^2/mol in the middle row represents a limiting case for a strongly emitting fuel (cross section of 2-methyl-pentane at 2965cm^{-1}), while the bottom figure represents the signal from an optically thick medium. As the absorption cross section increases wings of emission close to the injector in the periphery of the jet become more apparent.

All simulations show that cold fuel issuing from the injector tip will not have mixed sufficiently with the hot ambient gases to emit strongly until 10 or 20mm downstream in the steady jet[**]. In the downstream region of the jet, the IR emission for the 70m^2/mol simulation is

[**]In the model, all fuel is treated as fully vaporized, including mixtures near the injector, which will have some liquid fuel remaining in the real jets. Transient vaporization effects are not included here, and extra time to vaporize the fuel may further delay emission signals.

strongest along the jet centerline and decreases radially toward the boundary of the jet as the fuel concentration decreases and the mixed temperature increases. The combination of decreasing concentration paired with increasing temperature results in a non-linear profile of the IR emission signal, with steeper gradients near the jet boundaries than fuel concentration. At the penetrating head of the jet, the fuel concentration gradients are even sharper than at the radial jet boundaries (Espey et al. 1997), such that the IR emission signal should also be very sharp. Hence, the simulation shows that the IR emission signal remains strong even near the jet boundary where fuel concentrations are low, such that the penetration of the jet boundary should be discernable in images of IR emission.

Note that an ensemble-averaged simulation will not perfectly represent the intensity of an image detected of the instantaneous field since it does not account for instantaneous mixing structures present in a real jet. Additionally, the simulation does not account for absorption and reflection from the windows, emission from the camera lens or other sources in the field of view, the quantum efficiency of the detector, exposure duration, etc., all of which will affect the detected IR emission signal strength, the overall resolution, and the signal to noise ratio of the acquired camera images.

4. Experimental Setup

ENGINE

The optical engine used in this study is a single-cylinder direct-injection 4-stroke diesel based on the Cummins N-series production line. In Figure 3, we depict the setup used for the initial vapor-penetration experiments with the IR camera and schlieren setup. A brief description of the engine and optical setup follows.

This single cylinder has a bore of 140mm and stroke of 152mm for a total displacement

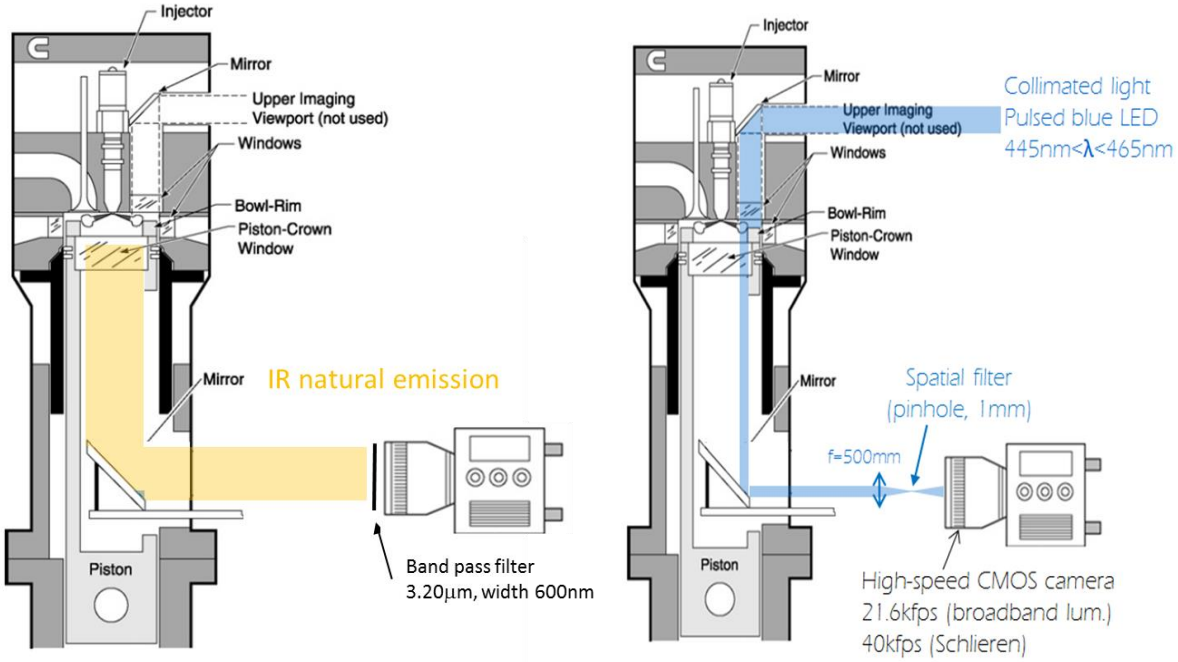

Figure 3 Extended piston heavy-duty optical engine schematic including IR and schlieren diagnostic setup

of 2.34L. The intake-port geometry yields a swirl ratio of 0.5 (low swirl). The upper cylinder-liner (black in Figure 3) can drop down from the head, allowing for rapid disassembly and cleaning of in-cylinder optical surfaces. Optical access is afforded by the extended piston with a flat piston-crown window (fused silica), viewed using a UV-enhanced aluminum mirror. One of

Table 1 Engine and Injector Specifications

Engine base type	Cummins N-14, DI Diesel	Fuel injector type	Common rail , solenoid-actuated Bosch CRI2.2
Number of cylinders	1	Cup (tip) type	Mini sac
Number of intake valves	2	Number of holes	7, equally spaced
Number of exhaust valves	1	Spray pattern included angle	148°
Swirl ratio	0.5	Nozzle orifice diameter, mm	0.141
Bore × Stroke, cm	13.97 × 15.24	Nozzle orifice L/D	5
		K factor	1.5
Bowl width, depth, cm	9.78, 1.55	Fuel injector type	Common rail , solenoid-actuated Bosch 'Spray B'
Displacement, liters	2.34	Cup (tip) type	Mini sac
Connecting rod length, cm	30.48	Number of holes	3, equally spaced
Replicated compression ratio†	16:1	Spray pattern included angle	145°
Geometric comp. ratio	11.22:1, set 1	Nozzle orifice diameter, mm	0.090
	10.75:1, set 2	Nozzle orifice L/D	11

† TDC conditions for a 16:1 compression ratio engine are produced in the optical engine by preheating and boosting the intake stream.

the exhaust valves has also been replaced with a window (fused silica) and UV-enhanced aluminum periscope mirror. One of the jets is aligned with this window to allow for schlieren measurements of the downstream portion of the jet, using the overlap of the cylinder-head and piston-crown windows, as depicted in Figure 3 (right). Specifications of the engine are summarized in Table 1. Detailed engine performance metrics for each run condition appear in Appendix A.

Table 2 Experiments Performed

Dataset		**1**	**2**
Injector		Spray B	Bosch CRI 2.2
# holes		3	7
Diameter	mm	0.090	0.141
Angle	°	146	148
P_{rail}	bar	1500, 1000	750
O_2	% vol.	0, 4	15
DSE*	ms	0.795	1.1
SSE	CAD	355	352
T_{tdc}	K	900	900
ρ_{tdc}	kg/m^3	15.2, 22.8	22.8
Speed	RPM	1200	1200
Fuel type		n-dodecane	n-dodecane

*DSE is the electronically commanded duration of solenoid energizing.

OPERATING CONDITIONS

The engine tests target two ambient-gas densities, 15.2kg/m^3 and 22.8kg/m^3, common to the ECN database at a single top dead center (TDC) temperature of 900K (TDC = 360CAD). The injection events do not occur in immediate succession; instead the engine is operated in a 1 fired to 9 motored cycle pattern. Due to limitations in the flow rate of nitrogen in our facility, it is not possible to achieve the higher density condition under non-combusting conditions with pure N_2 (0% O_2). To achieve the higher density condition without affecting the heat release we add 19% air, yielding 4% O_2 in the resulting intake stream. This achieves the higher density condition without detectable heat release, but images reveal sensitivity in the schlieren measurements, which will be discussed more in depth below. All experimental variations are listed in Table 2. Dataset 1 details the Spray B experiments using a demonstration IR camera available in the lab for only a few hours. Two operating conditions (4% and 0% O_2) are tested with this optical setup at a spatial resolution of 2.2pix/mm.

In dataset 2, we gather imaging data from a newly acquired IR camera model. Unfortunately, the Spray-B injector was not available at the same time as the new IR camera, so results with the Bosch CRI 2.2 injector are presented instead. For other reasons, we are also

interested in the spray impacting the wall using these data (not detailed here), and so a small window cut-out is added to the bowl rim, reducing the geometric compression ratio from 11.22 to 10.75. In the data shown, this cut-out is away from the periscope window and shouldn't impact the measured penetration. 15% O_2 (representing dilute combustion) is selected. The imaging setup also provides a higher spatial resolution of 4.2pix/mm.

SCHLIEREN AND INFRARED IMAGING

A summary of the LED-schlieren and IR emission techniques we employ in this study, along with a sample image for each, appears as Figure 4. The LED lighting and Phantom® v7.1 camera system has been detailed elsewhere (Eagle and Musculus, 2014), but not in a schlieren configuration. Details relevant to schlieren and two different IR cameras are included below.

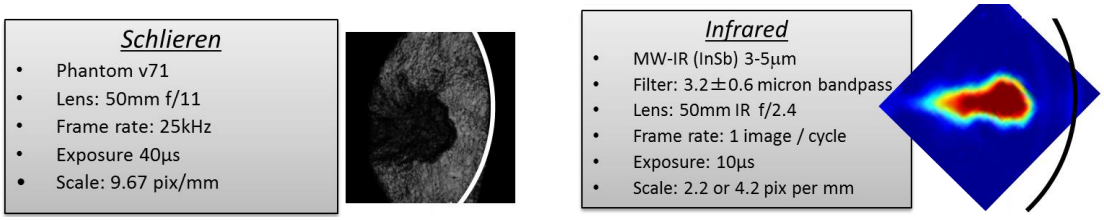

Figure 4 Vapor penetration detection diagnostics and setup for the two techniques. (2.2 pix/mm image shown for IR)

In this experiment, we acquire schlieren images of one penetrating diesel jet passing between the cylinder head and piston window as shown in Figure 3. The schlieren light source is a blue (445-465 nm) LED. The LED is driven in a burst mode producing 200 pulses of duration 5µs at a frequency of 25kfps. The shorter duty cycle and duration allows for instantaneous currents that temporarily 'overdrive' the LED and provide more incident light than it could tolerate at a 100% duty cycle. The LED source is focused through a 1mm diameter pinhole by a 50mm camera lens. The light passing through the pinhole is collimated using a 500mm spherical lens placed one focal length from the pinhole. The resulting collimated beam is directed through the engine as depicted in Figure 3. In front of the camera, another 500mm spherical lens focuses the light transmitted through then engine to the bright-field schlieren stop, another 1mm diameter pinhole. The camera lens object distance is set to infinity, and the f-stop is set to f/11. The field of view is the intersection of the periscope and piston windows, resulting in imaging of the downstream portion of one jet, roughly 30mm to 50mm from the injector orifice, which passes below the cylinder-head window before impinging on the bowl wall. The camera frame rate is 25kfps and the exposure duration is 40µs (though the effective exposure duration is set by the LED pulse duration of 5µs), corresponding to 1 image each 0.29 CAD at 1200rpm. The size of the images is 128x256pixels, at a scale of 9.67pxl/mm. The average penetration data shown in the next section are computed ensemble averages from thirty cycles.

We use two different IR cameras during the course of this campaign. The first set of data is from a demonstration camera, which was only available for only a few hours. It is a Telops Tel1000 MWIR with a customized detector capable of 1.5-5 micron detection. We since acquired a dedicated IR camera for the laboratory. It is a Thermal Scientific mid-wave infrared (TS-MWIR) from Telops with a 3-5 micron detection range. Both cameras house a 512x640 InSb focal plane array (FPA). The maximum full-frame acquisition rate of the cameras is 300Hz, which is too slow relative to the jet penetration times to acquire more than one useful image per cycle. Hence, a single image is acquired per cycle at different phases in the jet penetration event, and images from different cycles at different phases are assembled to yield the full penetration dataset. Consecutive injector-fired cycles are imaged between 3 and 20 CAD after the start of

solenoid energizing at 1 CAD resolution. The injector has a hydraulic delay of ~2.5CAD (measured hydraulic delays for each test are in appendix A, top-right panels). A 50mm f/2.4 3-5 micron Janos IR lens resolves the entire cylinder bowl at a resolution of 2.2 pix/mm. The camera exposure duration is set to 10μs. The second set of data has an improved resolution[††] of 4.2pix/mm and the same exposure duration. The camera lens is always fitted with a 'hot filter' (no active cooling) centered at 3.2 microns having a filter width of 0.6 microns. This provides the band gap through the window where fused silica transmits and collects emission from the expected 3.4 micron asymmetric stretch from CH_2 groups. This band avoids interference from CO_2, although H_2O bands centered near 3 microns may also contribute to emission in the reacting cases. A camera-specific non-uniformity correction (NUC) supplied by the camera manufacturer is applied to the images shown to remove systematic error in the FPA detector efficiency. The 512x640 detector array has <1% bad pixels, which is typical for these arrays, and these are replaced in the images shown using a local interpolation scheme.

IMAGE PROCESSING

Many features from imaging sprays and jets can be used for characterization, see e.g. Soid and Zainal (2011). We are primarily interested in the maximum penetration of the vapor-fuel jet resulting from the injection of the liquid fuel. The vapor penetration is analyzed using a standard ECN methodology currently available for download (Picket 2014). The penetration calculation methodology is as follows.

First, the locations of the injector and individual orifices in each image are determined. Then each image is normalized by its maximum recorded intensity and the normalized image is converted to binary using an intensity thresholding routine, im2bw.m, from Matlab®'s image processing toolbox (Mathworks 2012). Here, the thresholds are 2% and 7% of maximum intensity for the IR and schlieren images, respectively. The boundary at the threshold intensity is identified using the ECN code jetboundary.m and the instantaneous vapor penetration is computed from a given pixel-to-mm scale factor. Finally, the timing of each image relative to the start of injection is determined from the known injector start of solenoid energizing (SSE), the injector hydraulic delay measured from the first detectable deviation in the high pressure fuel rail, and the camera trigger. Past work has shown that this measured delay is well correlated with the start of visible fuel injection (Bobba, Musculus, and Neel 2010).

The largest temporal uncertainties in the image processing come from variability in the hydraulic delay for different orifice geometries and different injectors[‡‡]. This value may also depend on fuel type, fuel rail pressure, and fuel rail temperature. The chosen intensity threshold for the image processing and any error in locating the origin of each spray orifice also potentially affect the reported penetration measurements, but these effects have been previously shown to be small (Eagle, Morris, and Wooldridge 2014).

DATA PROCESSING

During the limited time that the IR demonstration camera was available, IR images were acquired only with a fuel rail pressure of 1000bar rather than the ECN standard 1500bar. Therefore, we add a procedure to scale the data using well-established dependencies so that the

[††] With our optical setup, we found that the IR camera is best focused by viewing the cylinder head with the engine static, using long exposure times (5s) with the 3.2 micron filter in place. Without the filter, thermal emission from the fused silica window, as well as a reflected image of the cold-stop, make proper focusing difficult.

[‡‡]measured data for the injector hydraulic delay is in the upper right corner in each plot of Appendix A, typically 2.1CAD for Spray B and 2.4CAD for the Bosch CRI2.2.

data can be compared more directly. We choose for comparison, schlieren data from the engine combustion network (ECN) single-orifice Spray A spanning the pressure conditions used here (Picket 2014). To compare these data, the scaling developed by Naber and Siebers (1996) for penetration, S, of a diesel jet issuing from an orifice of diameter d_o with fuel density ρ_f, ambient density ρ_a, fuel pressure P_f, and ambient pressure P_a, is applied:

$$x^+ = \frac{\sqrt{C_a}\cdot d_o\sqrt{\rho_f/\rho_a}}{a\cdot\tan(\theta/2)} \quad (7)$$

$$t^+ = \frac{x^+}{U_f} \quad (8)$$

$$U_f = C_v\sqrt{2\left(\frac{P_f-P_a}{\rho_f}\right)} \quad (9)$$

The correlations require four experimentally derived correction factors: the area contraction coefficient, C_a, (value 0.7); two parameters related to the jet dispersion, an arbitrary constant, a, (value 0.66) and spreading angle, θ; and the orifice velocity coefficient, C_v, (value 0.66) to correct the predicted velocity from the Bernoulli formula in Eq. 9.

All cases are rescaled as $\left(x = S_m\cdot {x^*}/{x^+}\ , t = t_m\cdot {t^*}/{t^+}\right)$ where S_m and t_m are the experimentally measured penetration rates and times, $x^+$and t^+ provide normalization with measured values for d_o, ρ_a, and P_f. Finally, $x^*$and t^* approximately represent a 0.09mm orifice injection at 1500bar into 900K and 22.8kg/m^3 TDC condition[§§]. A constant jet spreading full-angle of 19[***] degrees for all injectors is also assumed for simplicity.

5. Results and Discussion

LOW-RESOLUTION IR IMAGES

The first set of data only uses a small region of the full field of view (200x200 pixels) of the camera (512x640). Example instantaneous IR vapor penetration images in pixel coordinates and arbitrary counts is shown in Figure 5. Details of the operating condition appear in appendix A, Figure 11. The maximum intensity registered by the camera in this configuration was sub-optimal, only 450 counts out of the full-scale range of 16383 counts (14 digital bits). Nevertheless, the IR emission intensity distribution in the images is similar to the predictions in Figure 2, with higher intensity along the jet centerline, and higher intensity downstream where the fuel is hotter and the line-of-sight path lengths are longer. Also, as described earlier, the gradients of the IR emission intensity near the head of the jet are sharper than along the side of the jet, likely due to the sharper fuel concentration gradients typical at the jet head. Hence, with sharp gradients and strong downstream signals, the IR emission images should be able to provide reliable penetration measurements of the jet head.

[§§] For example, assume a measured penetration for 0% O_2 at 8.5 CAD ASE S_m = 40mm at $t_m = (8.5-2.1)*140 =$ 0.896ms for the IR camera Spray B (recall IR data is at 1000bar fuel rail pressure and 15.2kg/m^3 ambient density). Since the orifices are the same size and we assume equal jet angles:

${x^*}/{x^+} = \sqrt{22.8/15.2} = 1.225$, and ${t^*}/{t^+} = {U_f^+x^*}/{U_f^*x^+} = \sqrt{22.8/15.2}\cdot\sqrt{1000/1500} = 1$ (a reasonable approximation for $U_f^+x^*/U_f^*x^+$ since $P_a \ll P_f$).

[***] compare 19.5 degrees for 950K at 15.5kg/m^3 with 18.18 degrees at 1000K 28.6kg/m^3

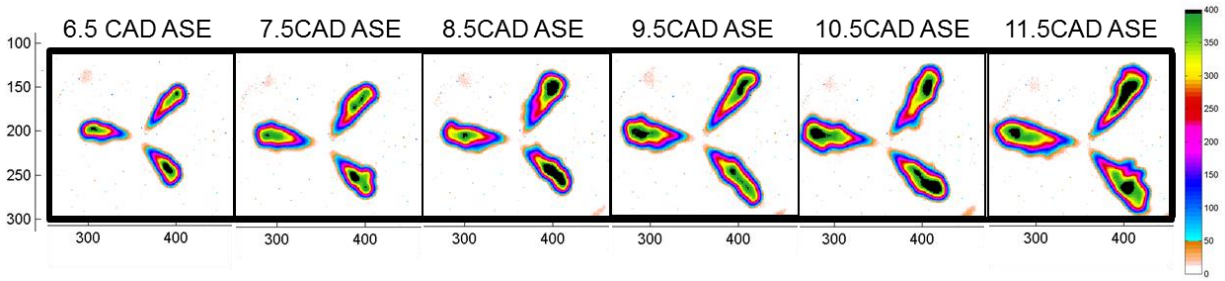

Figure 5 Sequence of IR camera images from 6.5 to 11.5 crank angle degrees (CAD) after the start of solenoid energizing (ASE). Images are from different injections. Operating condition as in Figure 11)

Although visible to the eye in the earliest instantaneous images (not shown), the first vapor penetration of relatively cold fuel in the IR (the data point missing from the IR camera at ~0.12ms in Figure 6) is below the threshold of detectability for the first penetrating spray using the ECN processing code. This is a common problem across all the IR measurements regardless of resolution and sensitivity. Adjustments to the detection scheme used for penetration in the ECN are likely necessary for IR camera data. This will be examined further in future work.

Quantification of the measured penetration data is compared in Figure 6. For times after injection less than about 0.7ms, the three-hole 'Spray B' in the engine using IR imaging penetrates more slowly than the Spray A case in the constant-volume chamber. Afterwards, both schlieren (when jet penetration becomes long enough to be visible through the ports in Figure 3) and IR data show the penetration in the engine exceeding the vessel. Comparing the two engine measurements, the IR camera shows an under-penetration of the average of the three jets. However, considerable scatter exists between the three individually measured data, and more work is required to evaluate these discrepancies. Uncertainty is partly introduced by the low spatial resolution. Another possibility is a registration error in the detection of the average start of injection (SOI), i.e, when fuel begins to emerge from the nozzle, used to synchronize the reported time in the comparisons. These issues are further discussed in the Limitations and Uncertainty section below.

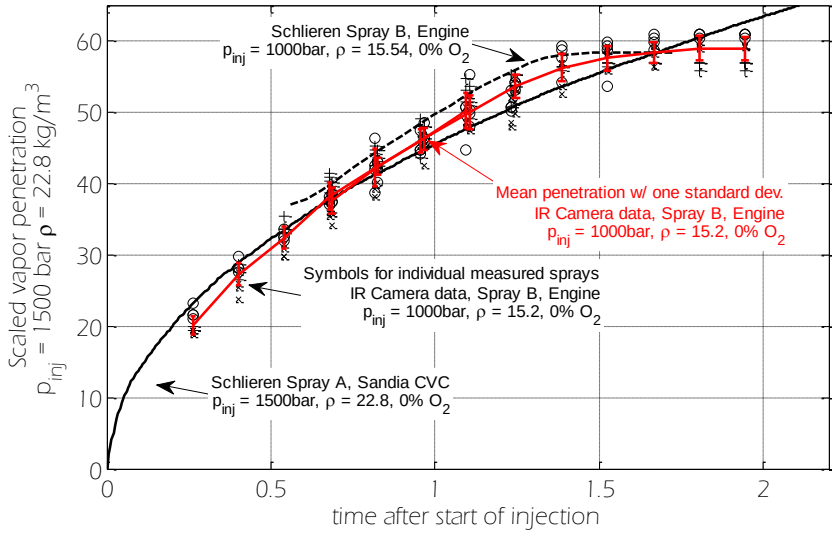

Figure 6 Scaled vapor penetration measurements. Black lines are from schlieren. Red line is ensemble average penetration from IR. Symbols are instantaneous IR from all three orifices.
Operating conditions: solid red line = Figure 11, dashed black line = Figure 13. Solid Black Line, ECN data.

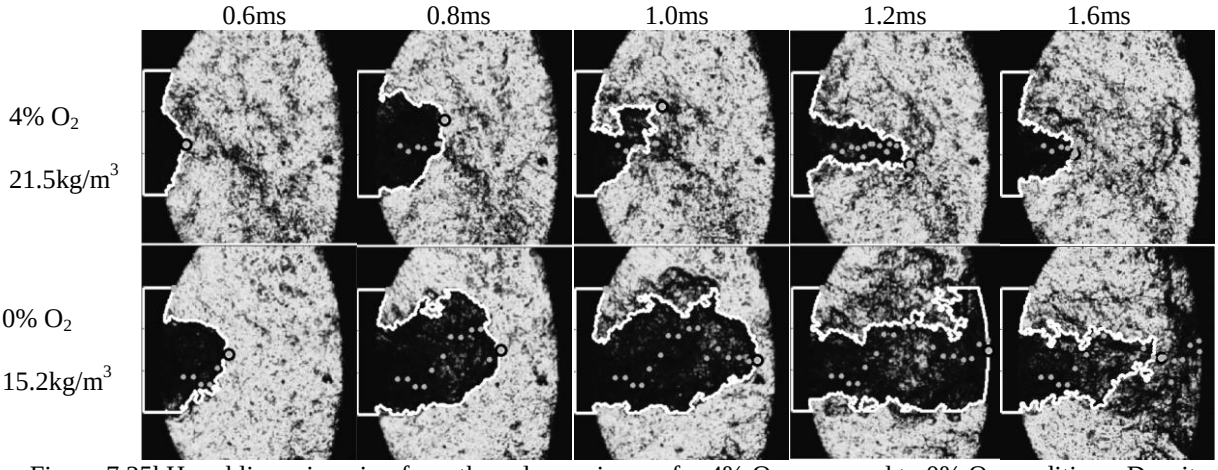

Figure 7 25kHz schlieren imaging from the valve periscope for 4% O_2 compared to 0% O_2 conditions. Density conditions are different, top = Figure 14, bottom = Figure 13, but both jets should penetrate to the bowl wall by 1.2ms. Grey dots represent previous maximum penetration to allow visual tracking of the spray tip.

LOW-TEMPERATURE REACTION

During reacting cases , it has recently been shown by formaldehyde planar laser-induced fluorescence and schlieren that the amplitude of schlieren variations in areas of low temperature reaction zones at the boundary of the jet decreases when first-stage "low-temperature" ignition reactions begin to occur, before suddenly becoming visible again after second-stage "high temperature" ignition reactions begin (Skeen, Manin, and Pickett 2015). Smoothing of the schlieren variations is described as "softening" because it hinders the ability to detect gradients. In Figure 7, image data is presented that confirms this result, even with very low ambient oxygen concentrations of 4%, compared to 0% O_2 concentration, at 0.6, 0.8, 1.0, 1.2, and 1.6ms after the start of injection. Prior to these observations, we expected that with no sensible heat release (compare top middle plots of Figure 113 with Figure 124 from Appendix A) that the progression of penetration using the schlieren technique would be the similar at 4% O_2 as at 0% O_2. Yet, the measured jet penetration progression in schlieren images (with our optical sensitivity) is significantly different. An overall reduction in schlieren signal at the jet periphery beyond 0.8ms in the 4% O_2 case is attributed to first-stage ignition reactions that yield a negligible change in the cylinder pressure. By the final image at 1.6ms, both jets should have reached the bowl wall. However, the 4% O_2 case, the measured penetration is never greater than 40mm. These results are quantified in Figure 8 as the dashed lines.

The resulting schlieren penetration in the engine is compared to the ensemble average of three cycles collected with IR between 0.3 and 1.6ms after the start of injection (aSOI) and two cases of schlieren penetration using the Spray A injector in a constant volume vessel. Note that the spray vessel has walls much further from the injector than in the engine, where the bowl wall is 49.3mm. As in Figure 6, all data are scaled to a common experimental condition as indicated in the axis label. Under non-reacting conditions, the penetration in the engine slightly exceeds that of the constant-volume vessel until the bowl wall is approached. The engine data track more closely with the reacting case for the data from the vessel.

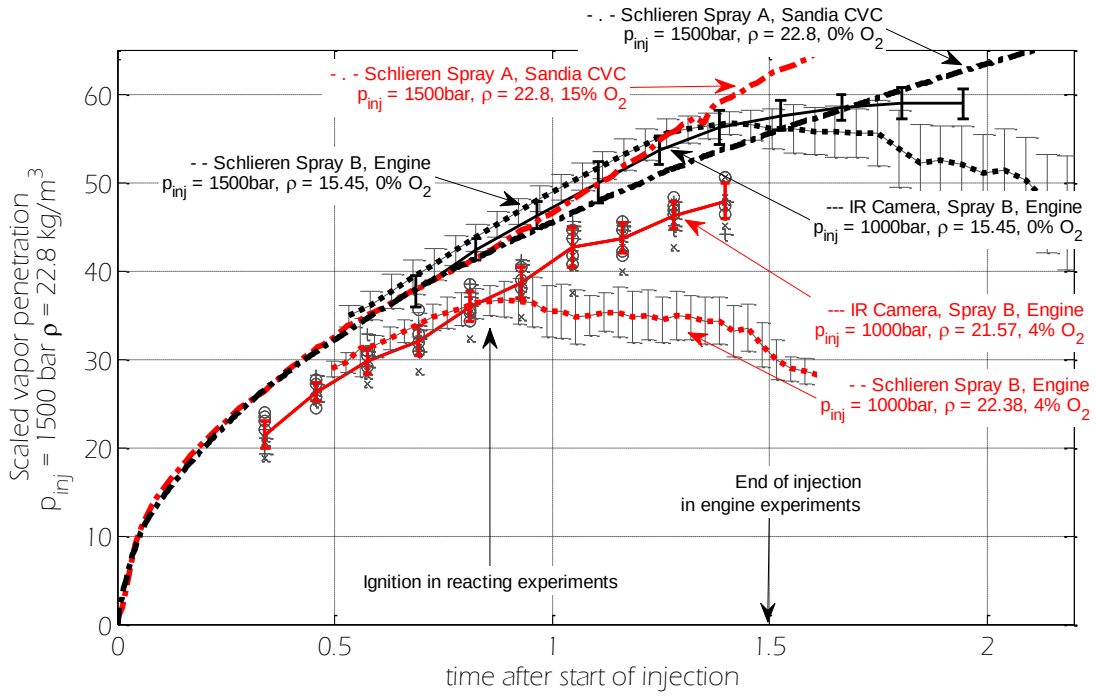

Figure 8 Scaled vapor penetration measurements at reacting (red) and non-reacting (black) conditions. Error bars indicate one measured standard deviation from the mean. Symbols are instantaneous IR penetration. IR: black = Figure 11, red = Figure 12, Engine schlieren: black = Figure 13 red = Figure 14.

Reacting data (red dashed dot) in the vessel at 15% O_2 begins penetrating further than non-reacting (black dashed dot) after the onset of ignition at 0.8ms. In the engine, the reacting jet penetration measured by both IR and schlieren is shorter than under non-reacting conditions. This preliminary result is in contradiction to previous experimental evidence at higher O_2 concentrations in the constant-volume vessel where reaction causes jet penetration to increase. Reduction in penetration of engine schlieren data due to gradient 'softening' is evident compared to the IR data at the same condition (lower set of red curves) after the onset of ignition reactions at 4% O_2. Further experiments would help to resolve these discrepancies, but unfortunately the camera and Spray B were available together only for a limited time.

HIGH RESOLUTION IR IMAGES

We received a second IR camera and more time to optimize its optical set-up, so a second round of injection images (dataset 2 in Table 2) is collected with a higher resolution of 4.2 pix/mm resolution. Since the Spray B injector was no longer available, a Bosch CRI2.2 injector was used. Compared to Spray A and Spray B, which have one and three 0.09mm orifices, respectively, the CRI2.2 injector has seven 0.14mm orifices. Recall that increasing the orifice diameter increases the penetration rate. For the conditions presented here, an ambient gas oxygen concentration of 15% by volume was used. Hence, the IR emission signal includes both hot-fuel emission as well as any combustion-generated luminosity that falls within the filter passband for images after ignition at 359.2 ± 0.9 CAD (7.2CAD after the start of solenoid energizing).

One series of images from this data set (dataset 2 in Table 2) is shown in Figure 9. The top row uses a color-scale range from zero to 2000 counts, while the bottom two rows use a range from zero to 12000 counts. Visible in the first row of images at 9 and 12o'clock are the intake valves. At 6o'clock is the exhaust valve and at 3o'clock is the periscope window that is in place of one of the exhaust valves (see Figure 3). In the bottom two rows, with the upper bound

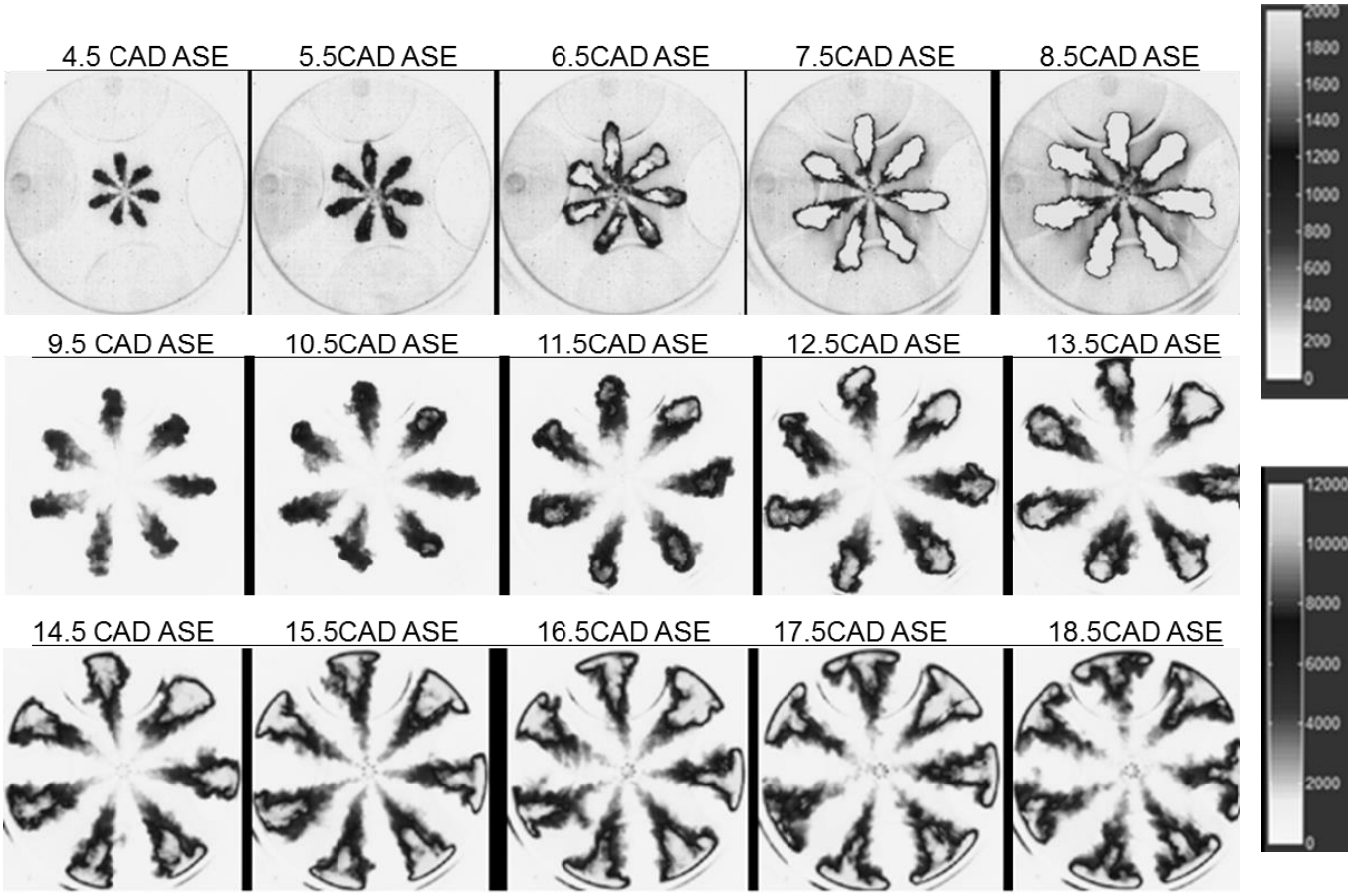

Figure 9 4.2pix/mm resolution of IR acquisition of subsequent fired cycles at the timings indicated. Duration of injection from visible scattering ends at 13.4CAD ASE, and ignition occurs near 13.4CAD ASE. Piston bowl edge visible in top row images is 97.8mm in diameter. Operating condition: 750bar injection into 22.74 kg/m^3 900K 15%O_2, details in appendix A Figure 15.

of the color scale increased to resolve higher peak IR emission signals, these features are no longer visible in the images as reproduced here, though they are still present in the data. These higher-resolution images (compared to Figure 5) show a sharp gradient of the IR emission intensity near the jet head, which again indicates that the IR data should provide good penetration measurements using intensity thresholdling techniques.

In the bottom row of images, IR emission intensity increases in the closest 20mm from the injector. Recession of the IR signal towards the injector is indicative of an increase in entrainment of hot ambient gas after the end of injection relative to the steady injection (Eagle et al. 2014). Under these reacting conditions at 15% O_2, there is also the possibly of reaction in these zones (Knox & Genzale 2015). If the observed recession is only due to entrainment, it demonstrates that detected emission preferentially occurs for lower concentration, hotter fuel. One other notable feature is the low-intensity spots at the injector orifices that become visible in the bottom row of images compared to the middle row. This emission is likely related to fuel dribble from the injector, which has been noted in previous visible imaging studies (Eagle & Musculus 2014).

A direct comparison of the measured vapor penetration of Spray B and the Bosch CRI2.2 appears in Figure 10. Again, for the purposes of direct comparison, the data have been scaled to the conditions indicated in the axis label, including a scaling for orifice size. Due to this scaling, the scaled bowl-wall position increases from 49.3mm (red) to 60.4mm (black) and 76.7mm

(blue). (The 750bar rail-pressure data have more significant stretching in the time dimension than at 1000bar.) For the region between 0.6 and 1ms, where the influence of the bowl wall is not evident, the agreement of measured penetration among the scaled data is fair, while it appears that the penetration rate of the larger orifice injector remains higher despite the applied scaling. Although the temporal scaling has slightly shifted the start of combustion, it appears that the penetration may indeed increase for this 15% O_2 case.

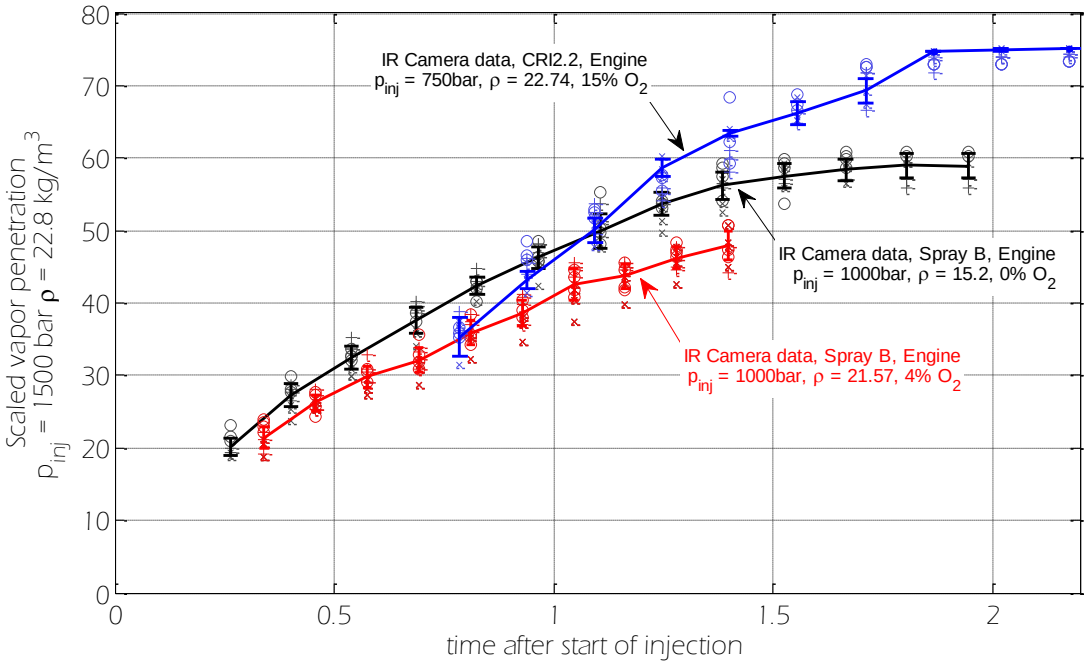

Figure 10 Comparison of three IR camera vapor penetration measurements.
Operating condition: Black = Figure 11, Red: Figure 12, Blue Figure 15.

6. LIMITATIONS, UNCERTAINTY AND FUTURE WORK

As previously mentioned, low absolute signal at times close to the start of injection made penetration measurements difficult. However, examining instantaneous images (not shown here) or by extrapolating the trend of the seven hole injector data, it appears that the initial penetration from the multi-hole nozzles is quite slow. Initial penetration may be reduced by extending the sac-pressure ramp-up time given the greater number of larger orifices providing pressure relief. However, the timescales over which any pressure relief effect lingers (or exists at all) has not been documented to the authors' knowledge. Detailed modeling of the internal dynamics for multi-orifice injectors or internal flow measurement is needed to confirm or disconfirm this supposition and to resolve the observed differences in penetration among injectors and operating conditions.

Only preliminary IR-camera data have been shown in this paper, and the operating conditions for disparate data do not match, requiring scaling adjustments to allow more direct comparisons of the data from multiple injectors and multiple facilities. As an example of comparisons with well-matched hardware and operating conditions, excellent agreement for measured vapor penetration in the engine is obtained between simultaneously acquired ultra-violet laser induced fuel fluorescence (UV-LIF) and schlieren measurements (L-M Malbec, personal communication, February 2015). Therefore, we soon plan to simultaneously measure vapor-fuel penetration using UV-LIF, visible schlieren, and IR emission. In particular, it will be

interesting to look for the comparison of data in reacting vs non-reacting cases that is still needed to confirm the enhanced penetration during reaction that was measured from a single orifice.

Additionally, the limited resolution of the penetration data both in time and space are an obvious place to improve in the future analysis. Timing registration errors relative to the start of injection for multi-hole vs single-hole injectors also will depend on the sac volume. Some consideration of whether the start of injection should be based on the injector command signal to account for variation in the internal injector dynamics, including nozzle sac filling time may be important to explaining the differences between single-hole and multi-hole nozzles. Thus far no consensus exists regarding how to interpret the start of injection besides the first visible fuel emitted from the injector. This visual cue tends to discard useful information regarding the internal nozzle dynamics manifesting as the injector hydraulic delay and treat spray/jet penetration as decoupled from the internal flow.

7. Summary and Conclusions

In this paper, we examined theoretical vapor-fuel emission in the IR using a simple model for emission and self-absorption. From the literature we verified the emission band centered near a wavelength of 3.4 microns is favorable for fuel-vapor penetration measurement. No modifications to our optical engine hardware, including the fused silica windows and UV-enhanced aluminum mirrors, were required to obtain IR emission images. IR vapor penetration data were collected at ambient oxygen percentages of 0%, 4%, and 15%. We also measured vapor penetration at 0% and 4% O_2 using a schlieren technique capable of imaging a single jet through a periscope in place of an exhaust valve. These data are the first measurements of their kind for the ECN database using an optical engine. All of the penetration data were scaled to a single orifice size, ambient density, and fuel-rail pressure so they could be compared to similar data collected in a constant volume vessel. The preliminary data presented here support the following conclusions:

- IR-emission signals from hot fuel-vapor jets are expected to produce good contrast at the jet head due to long path lengths and a favorable non-linear variation of the IR emission signal with decreasing fuel concentration near the jet boundaries due to increased mixture temperature (Figure 2 and 3).
- The IR technique at 3.4 microns is demonstrated as viable for vapor penetration measurement at 2.2 pix/mm and 4.2 pix/mm resolutions and 10μs exposure times (Figure 5 and 9). More features characteristic of an instantaneous penetrating jet, including sharp boundaries at the jet head, are visible in the high-resolution images.
- Based on the scaled penetration data, the initial penetration for the three-hole Spray B injector is slower compared to the single-hole Spray A, but the penetration rate increases quickly and the scaled penetration of Spray B in the engine overtakes the scaled penetration of Spray A from the constant-volume vessel (Figure 6). Also, in general, the IR penetration is slightly shorter than measured by the schlieren imaging. Both of these conclusions are based on preliminary data that were not acquired simultaneously, however, and should be confirmed using simultaneous measurements.
- Confirming the work of other authors, we see ‘softened’ schlieren effects, but even at a very low ambient O_2 concentration of 4%. As a result, schlieren imaging in regions of low-temperature reaction (first stage ignition in the head of the jet) may not provide a reliable measure of penetration (Figure 7). Penetration measurement based on IR emission remains robust for this low ambient O_2 concentration (Figure 7).

- Recession of IR signal back to injector after the end of injection and prominence of signal from apparent fuel dribble indicates that the IR diagnostic can be sensitive fuel at both hot, low-concentration and warm high-concentrations (Figure 9).
- When properly rescaled, we see fair agreement in the data collected in the IR at a variety of conditions (Figure 10).

8. Acknowledgements

The authors wish to thank Sandians Chris Carlen for his efforts in the design and manufacturing of ultra-fast LEDs and David Cicone for technical support. The research was performed at the Combustion Research Facility, Sandia National Laboratories, in Livermore, California. Sandia is a multi-program laboratory operated by Sandia Corporation, a Lockheed Martin Company, for the United States Department of Energy's National Nuclear Security Administration under contract DE-AC04-94AL85000.

Disclaimer of Liability

9. References

Agnew, W G, J T Agnew, and K Wark. 1955. “Infrared Emission from Cool Flames Stabilized Cool Flames; Engine Cool Flame Reactions; Gas Temperatures Deduced from Infrared Emission.” *Proc. Combustion Inst.* 5 (1): 766–778.

Alden, Marcus, Joakim Bood, Zhongshan Li, and Mattias Richter. 2011. “Visualization and Understanding of Combustion Processes Using Spatially and Temporally Resolved Laser Diagnostic Techniques.” *Proc. Combustion Inst.* 33: 69–97. doi:10.1016/j.proci.2010.09.004.

Bekefi, George, and Alan Barrett. 1982. *Electromagnetic Vibrations, Waves, and Radiation*. Third Edit. MIT Press.

Blessinger, Matthew, Julien Manin, Scott A Skeen, Maarten Meijer, Scott Parrish, and Lyle M Pickett. 2014. “Quantitative Mixing Measurements and Stochastic Variability of a Vaporizing Gasoline Direct-Injection Spray.” *International Journal of Engine Research*. doi:10.1177/1468087414531971.

Bobba, Mohan, Mark Musculus, and Wiley Neel. 2010. “Effect of Post Injections on In-Cylinder and Exhaust Soot for Low-Temperature Combustion in a Heavy- Duty Diesel Engine.” *SAE Int. J. Engines* 3 (1): 496–516.

Eagle, W E, and Mark P B Musculus. 2014. “Cinema - Stereo Imaging of Fuel Dribble after the End of Injection in an Optical Heavy - Duty Diesel Engine.” In *THIESEL 2014 Conference on Thermo- and Fluid Dynamic Processes in Direct Injection Engines*, 1–20.

Eagle, W E, Mark P B Musculus, L-M C Malbec, and G Bruneaux. 2014. “Measuring Transient Entrainment Rates of a Confined Vaporizing Diesel Jet.” In *ILASS Americas 26th Annual Conference on Liquid Atomization and Spray Systems, Portland, OR, May 2014*.

Eagle, W Ethan, Steven B Morris, and Margaret S. Wooldridge. 2014. “High-Speed Imaging of Transient Diesel Spray Behavior during High Pressure Injection of a Multi-Hole Fuel Injector.” *Fuel* 116: 299–309. doi:10.1016/j.fuel.2013.07.120.

Espey, Christoph, John Dec, Thomas Litzinger, and Domenic Santavicca. 1997. “Planar Laser Rayleigh Scattering for Quantitative Vapor-Fuel Imaging in a Diesel Jet.” *Combustion and Flame* 109 (1-2): 65–86.

Heywood, J B. 1988. *Internal Combustion Engine Fundamentals*. New York, NY: McGraw-Hill.

Janis.com. 2015. “Window Transmission Curves.” http://www.janis.com/products/AccessoriesandAncillaryEquipment/WindowTransmissionCurves.aspx.

Jansons, M, S Lin, T Fang, and K T Rhee. 2000. “Visualization of Preflame and Combustion Reactions in Engine Cylinders.” *SAE Technical Paper*: 2000–01–1800.

Jansons, M, S Lin, and K T Rhee. 2008. “Infrared Spectral Analysis of Engine Preflame Emission.” *International Journal of Engine Research* 9: 215–237. doi:10.1243/14680874JER00408.

Kawahara, Nobuyuki, Eiji Tomita, Atsushi Ohtsuki, and Yuzo Aoyagi. 2011. “Cycle-Resolved Residual Gas Concentration Measurement inside a Heavy-Duty Diesel Engine Using Infrared Laser Absorption.” *Proc. Combustion Inst.* 33 (2): 2903–2910. doi:10.1016/j.proci.2010.07.017. http://dx.doi.org/10.1016/j.proci.2010.07.017.

Klingbeil, Adam E, Jay B Jeffries, and Ronald K Hanson. 2007. “Temperature-Dependent Mid-IR Absorption Spectra of Gaseous Hydrocarbons.” *Journal of Quantitative Spectroscopy and Radiative Transfer* 107: 407–420. doi:10.1016/j.jqsrt.2007.03.004.

Klingbeil, Adam E, Jason M Porter, Jay B Jeffries, and Ronald K Hanson. 2009. “Two-Wavelength Mid-IR Absorption Diagnostic for Simultaneous Measurement of Temperature and Hydrocarbon Fuel Concentration.” *Proc. Combustion Inst.* 32 (1): 821–829. doi:10.1016/j.proci.2008.06.058. http://dx.doi.org/10.1016/j.proci.2008.06.058.

Knox, Benjamin W, and Caroline L Genzale. 2015. “Combustion Recession after End of Injection in Diesel Sprays.” In *SAE World Congress*, 2015–01–0797.

Luo, Xi, Xin Yu, and Marcis Jansons. 2015. “Simultaneous In-Cylinder Surface Temperature Measurements with Thermocouple, Laser-Induced Phosphorescence, and Dual Wavelength Infrared Diagnostic Techniques in an Optical Engine.” *SAE Technical Paper*: 2015–01–1658.

Mancaruso, Ezio, Luigi Sequino, and Bianca Maria Vaglieco. 2014. “IR Digital Imaging for Analysing in-Cylinder Combustion Process in Transparent Diesel Engine.” In *2014 Fotonica AEIT Italian Conference on Photonics Technology*.

Mancaruso, Ezio, Bianca Maria Vaglieco, and Luigi Sequino. 2015. “Using 2d Infrared Imaging for the Analysis of Non-Conventional Fuels Combustion in a Diesel Engine.” *SAE Technical Paper*: 2015–01–1646.

Mathworks. 2012. “Matlab.”

Musculus, Mark P B, and Kyle Kattke. 2009. “Entrainment Waves in Diesel Jets.” *SAE Int. J. Engines* 2 (1): 1170–1193. doi:10.4271/2009-01-0849.

Naber, Jeffrey D, and Dennis L Siebers. 1996. “Effects of Gas Density and Vaporization on Penetration and Dispersion of Diesel Sprays.” *SAE Technical Paper*: 960034.

Picket, Lyle M. 2014. “Engine Combustion Network.” *Sandia National Laboratories*. http://www.sandia.gov/ecn/.

Pickett, Lyle M, Caroline L Genzale, Dennis L Siebers, and Mark P B Musculus. 2012. “Relationship Between Diesel Fuel Spray Vapor Penetration / Dispersion and Local Fuel Mixture Fraction” 4 (1). doi:10.4271/2011-01-0686.

Rothman, L S, C P Rinsland, A Goldman, S T Massie, D P Edwards, J-M Flaud, A Perrin, et al. 1998. “The Hitran Molecular Spectroscopic Database and Hawks (hitran Atmospheric Workstation): 1996 EDITION.” *Journal of Quantitative Spectroscopy and Radiative Transfer* 60 (5): 665–710.

Schulz, Florian, Jürgen Schmidt, Andreas Kufferath, and Wolfgang Samenfink. 2014. “Gasoline Wall Films and Spray / Wall Interaction Analyzed by Infrared Thermography.” *SAE Int. J. Engines* 7 (3): 2014–01–1446. doi:10.4271/2014-01-1446.

Settles, G S. 2001. *Schlieren and Shadowgraph Techniques*. Berlin, Germany: Springer-Verlag.

Skeen, Scott A, Julien Manin, and Lyle M Pickett. 2015. “Simultaneous Formaldehyde PLIF and High-Speed Schlieren Imaging for Ignition Visualization in High-Pressure Spray Flames.” *Proc. Combustion Inst.* 35 (3): 3167–3174. doi:10.1016/j.proci.2014.06.040. http://dx.doi.org/10.1016/j.proci.2014.06.040.

Soid, S N, and Z A Zainal. 2011. “Spray and Combustion Characterization for Internal Combustion Engines Using Optical Measuring Techniques – A Review.” *Energy* 36 (2): 724–741. doi:10.1016/j.energy.2010.11.022.

Squibb, Cody William, Harold Schock, Thomas Stuecken, Mulyanto Poort, Kyle Crayne, Charles Gray, and Fakhri Hamady. 2011. “A Demonstration of Simultaneous Infrared and Visible Imaging Techniques with Pressure Data in an Optically Accessible Diesel Engine Operating at Part Load with High EGR.” *SAE Technical Paper*: 2011–01–1395. doi:10.4271/2011-01-1395.

Tomita, Eiji, Nobuyuki Kawahara, and Atsushi Nishiyama. 2003. “In Situ Measurement of Hydrocarbon Fuel Concentration near a Spark Plug in an Engine Cylinder Using the 3 . 392 M M Infrared Laser Absorption Method : Application to an Actual Engine.” *Measurement Science and Technology* 14: 1357–1363.

Appendix A

For all operating conditions, cylinder pressure, fuel rail pressure, and injector current are digitized and recorded at 1/4 crank-angle-degree (CAD) increments, simultaneously with the acquisition of the optical data. Other data including fuel return temperature after the injector, engine block coolant temperature, engine RPM, and intake air temperature and mass flow rate, are separately recorded each at 1s intervals. The apparent heat release rate (AHRR) is calculated from ensemble-averaged pressure data using an air-standard first-law analysis e.g., Heywood (1988). Prior to calculating the AHRR, the pressure data are smoothed using a Fourier series low-pass filter with a Gaussian roll-off function having a transmission of 100 % from 0 to 800 Hz and dropping to 1 % at 3360 Hz. We selected these cut-off frequencies to remove acoustic ringing in the cylinder pressure data, while retaining the general features of the AHRR. Using these filter parameters, the apparent start of combustion (SOC), indicated by the first zero-crossing of AHRR, is typically advanced from that for the unfiltered data up to 70 microseconds, depending on the size of the premixed burn. Additionally, the peak of the premixed burn spike in the filtered AHRR is reduced by as much as a factor of 2, while its width is increased by as much as a factor of 2. The apparent energy released during the premixed burn (area under the AHRR curve), however, is virtually unchanged by this filtering technique.

In the absence of ignition, some metrics typically assessed are instead left blank. Plots for the SOC are therefore set to zero. Maximum AHRR and gross indicated mean effective pressure (gIMEP) should not evaluated as meaningful engine output in non-reacting cases, but are useful to assess the repeatability of data and so their computed values are not removed.

In the figures of the appendix, we plot the engine data processing routine results as following.

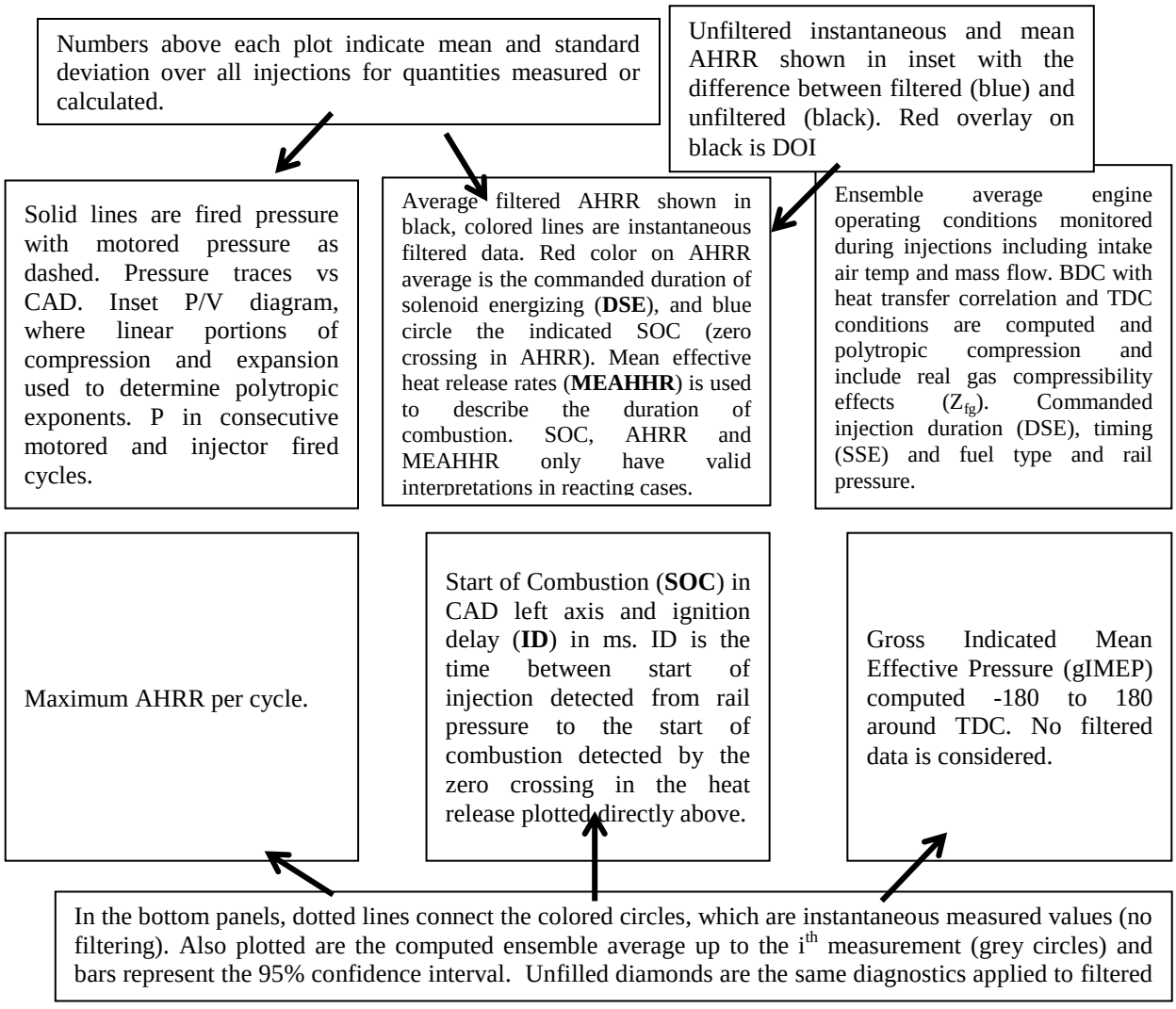

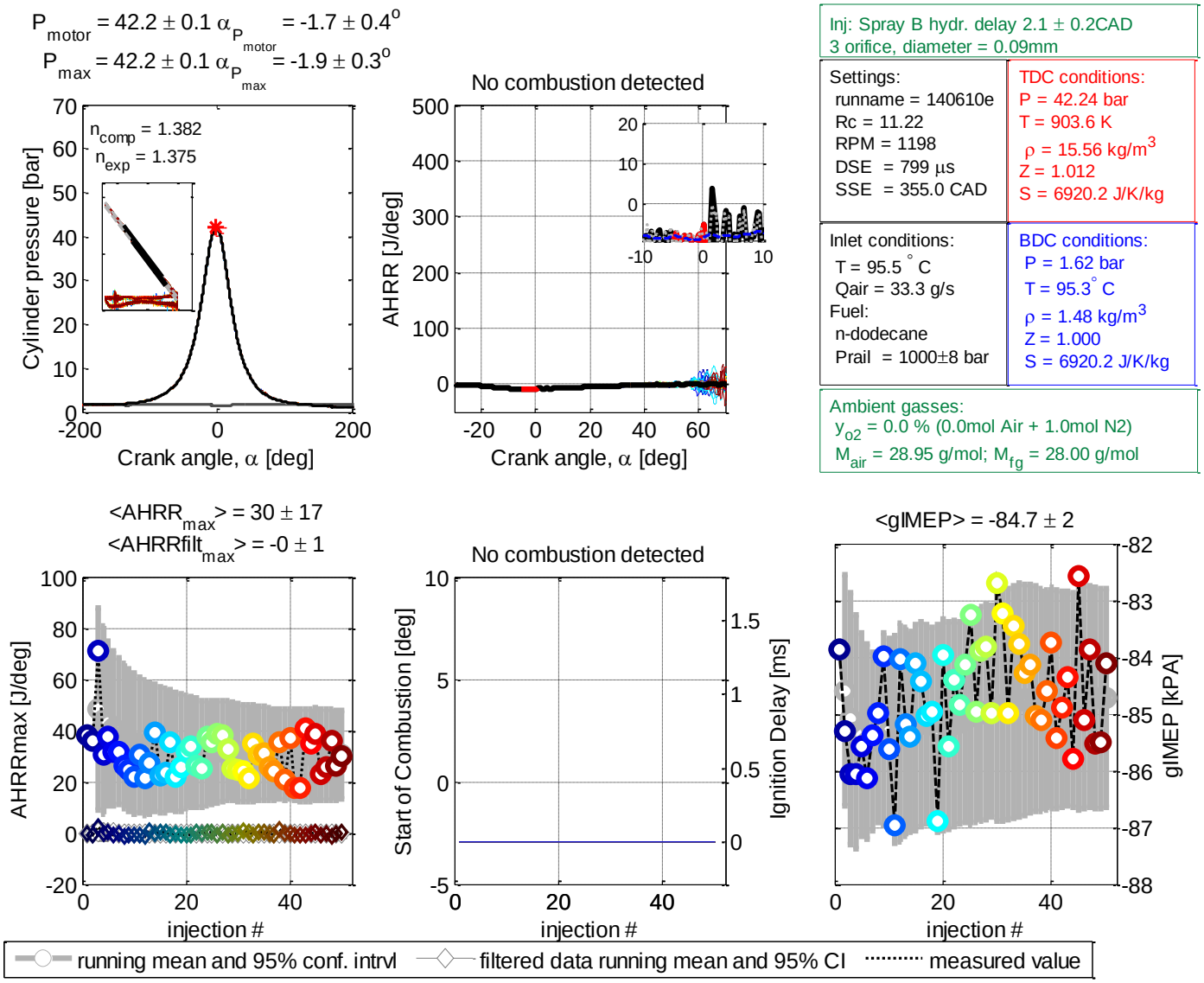

Figure 11 Engine operating conditions for IR Camera Data targeting 15.5 kg/m3 900K for penetration data shown in Figure 6, 6, 8, and 10. No positive AHRR, no ignition delay, and negative gIMEP are detected because engine was run with 0% O_2.

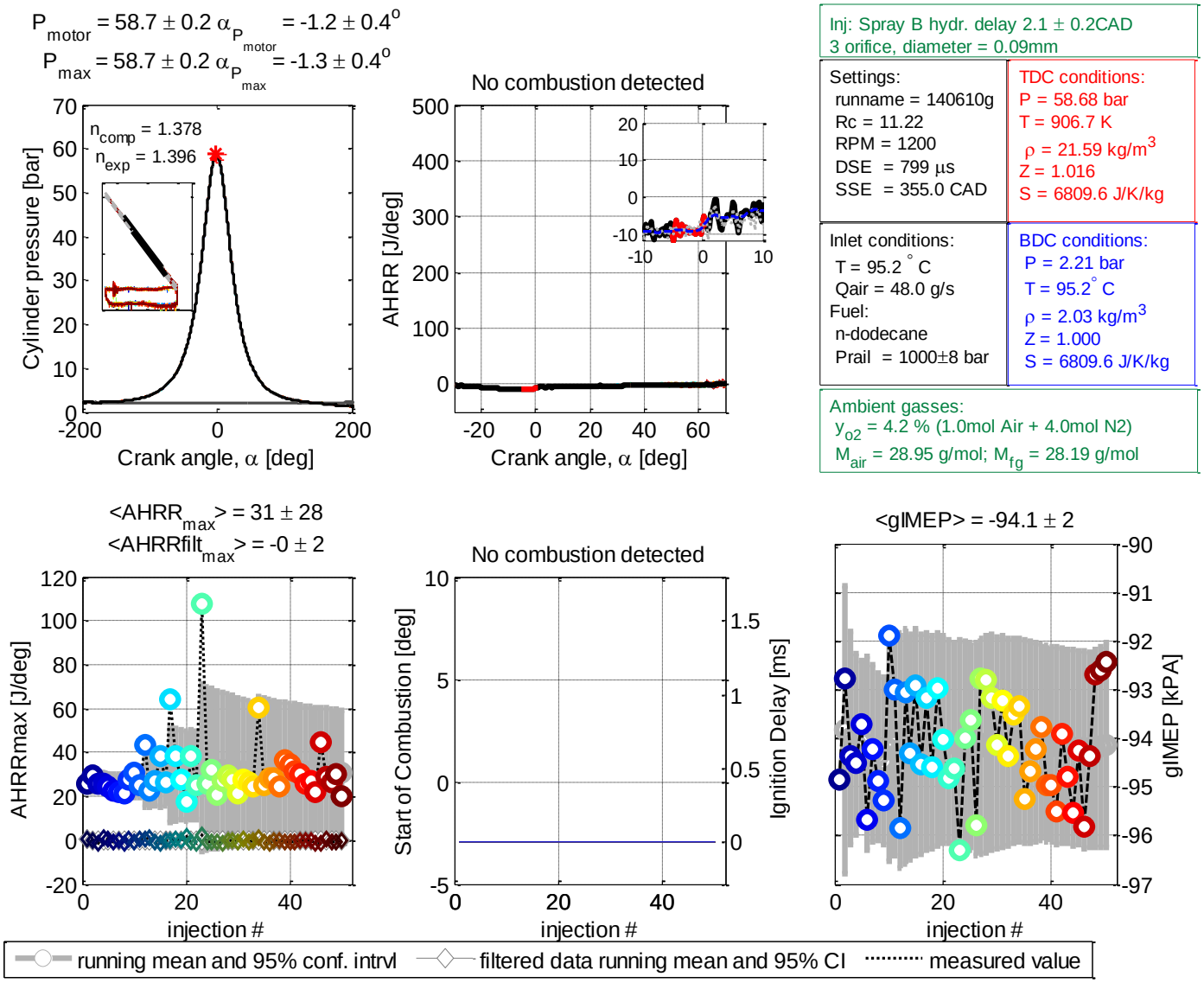

Figure 12 Engine operating conditions for IR vapor penetration targeting TDC 22.8 kg/m^3 for penetration data shown in Figure 6, 8, and 10. No AHRR or ignition delay and negative gIMEP are detected because engine was run with 0% O_2.

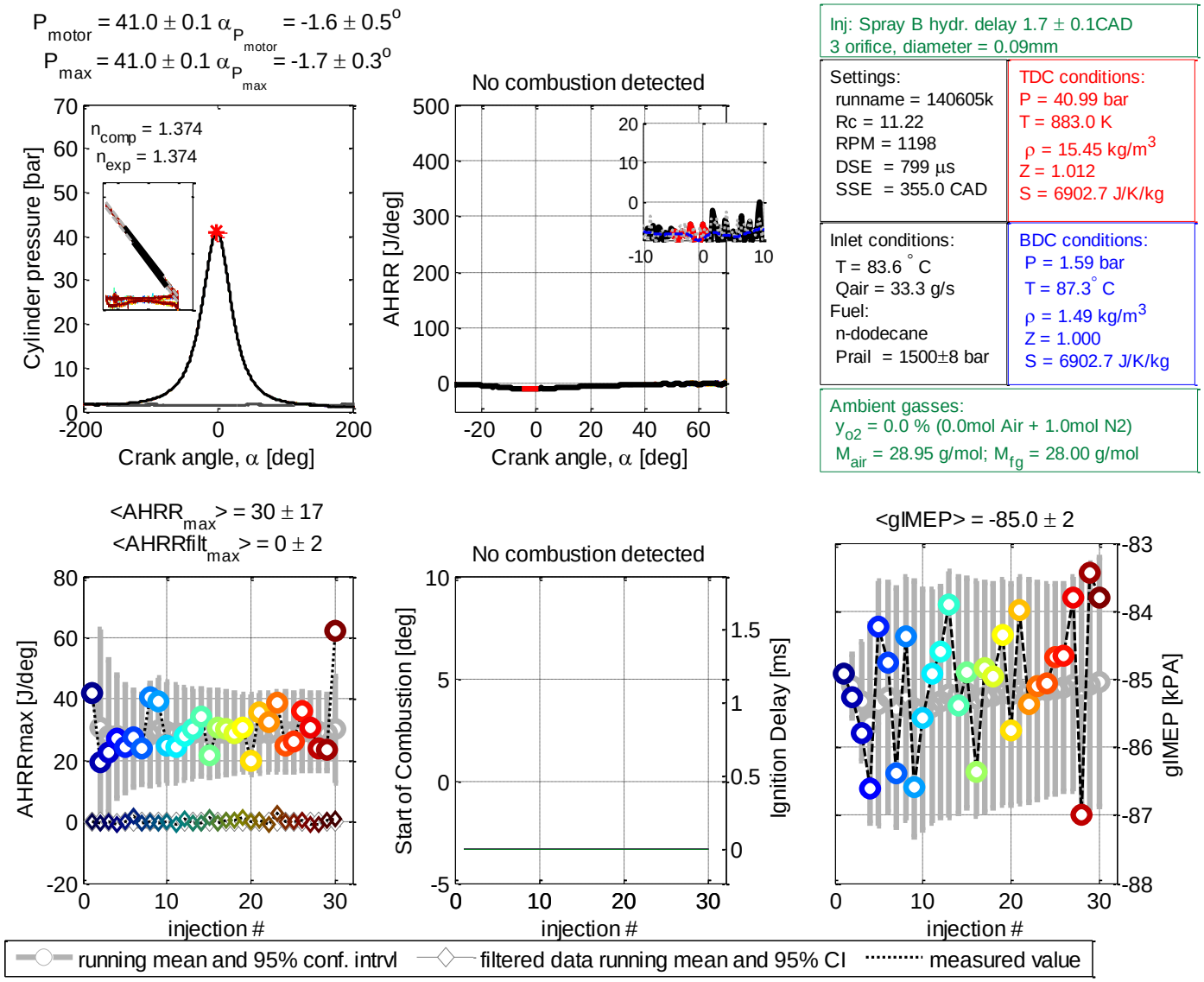

Figure 13 Engine operating conditions for schlieren vapor penetration targeting TDC 22.8 kg/m^3 900K for penetration data shown in Figure 6, 7, and 8. No positive AHRR, no ignition delay, and negative gIMEP are detected because engine was run with 4% O_2.

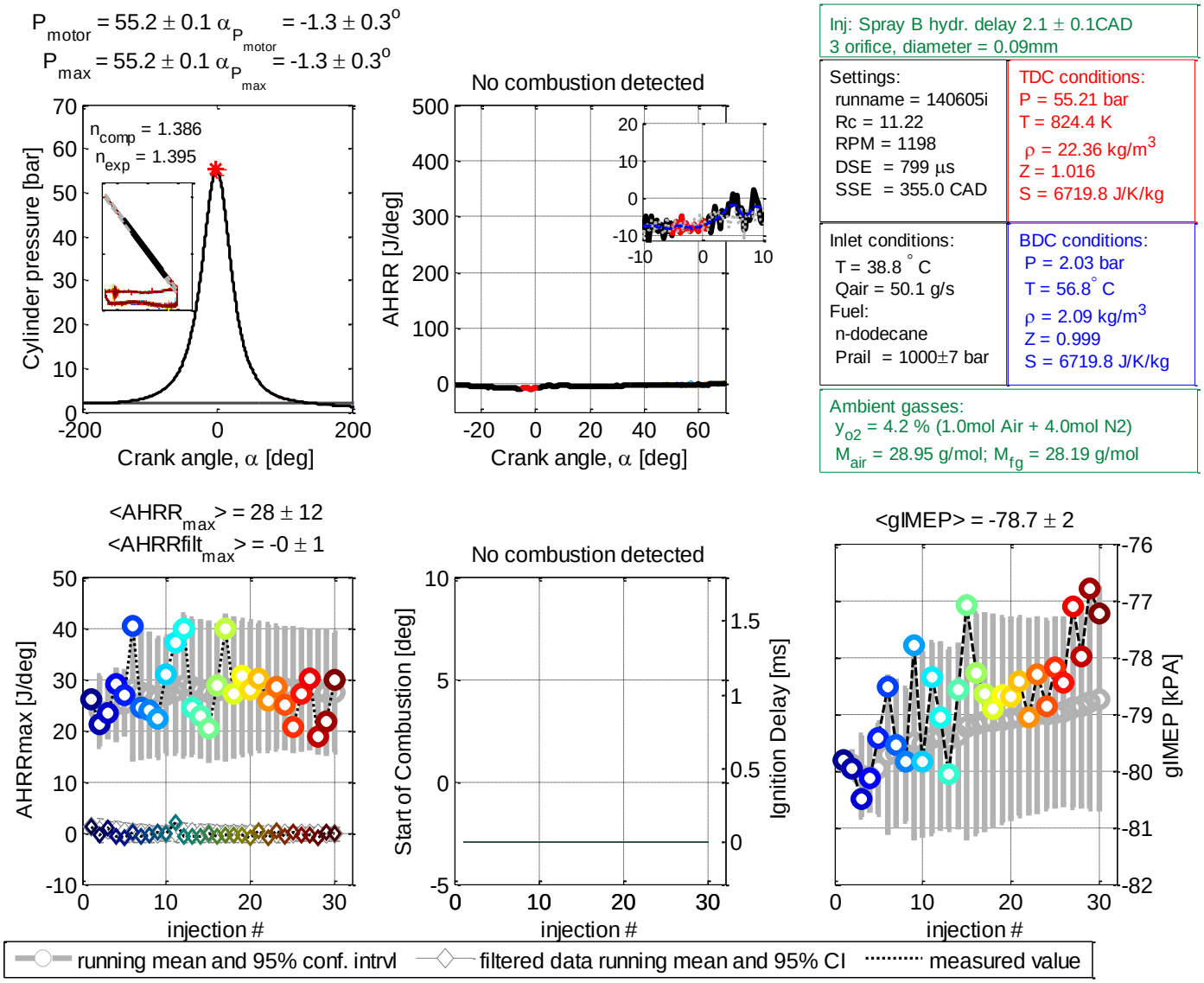

Figure 14 Engine operating conditions for schlieren vapor penetration targeting TDC 15.2kg/m^3 900K for penetration data shown in Figures 7 and 8. No AHRR or ignition delay and negative gIMEP are detected because engine was run with 4% O_2.

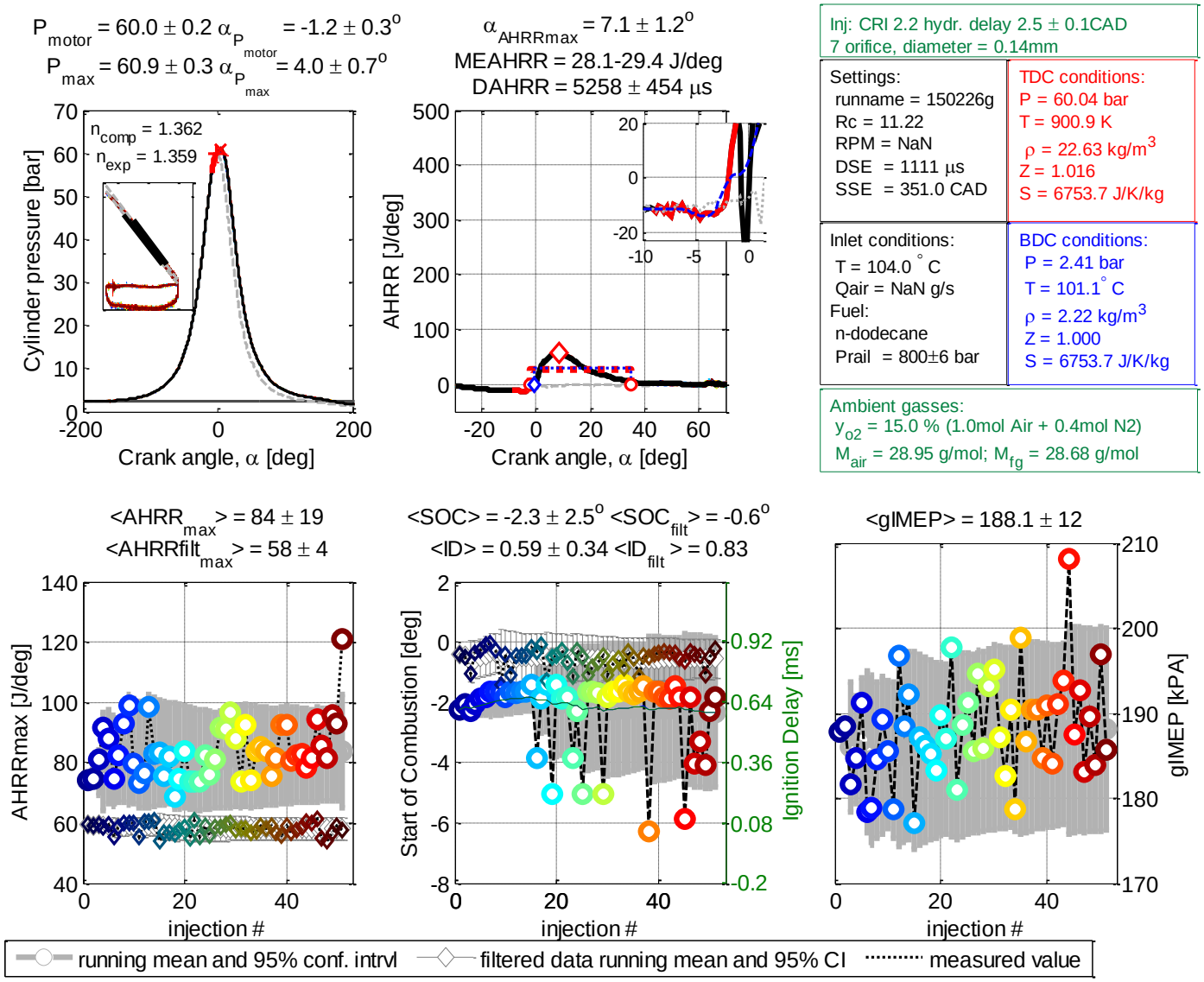

Figure 15 Engine operating conditions for IR camera imaging TDC 22.8kg/m^3 900K for imaging data shown in Figure 9 and 10. Engine operation targeted 15% O_2.